

# Levitational Image Cytometry with Temporal Resolution

Savas Tasoglu, Joseph A. Khoory, Huseyin C. Tekin, Clemence Thomas,  
Antoine E. Karnoub, Ionita C. Ghiran,\* and Utkan Demirci\*

A wide variety of cellular processes, both physiological and pathological, are accompanied by transient or permanent changes in a cell's fundamental characteristics as a biological material: i) volumetric mass density or ii) magnetic signature due to formation or quenching of intracellular paramagnetic reactive species such as, reactive oxygen species (ROS), and reactive nitrogen species (RNS). These events include cell-cycle stage,<sup>[1]</sup> differentiation,<sup>[2]</sup> cell-death (apoptosis/necrosis),<sup>[3]</sup> malignancy, disease state,<sup>[4]</sup> activation, phagocytosis, in vivo and ex vivo cell aging (e.g., red blood cells), viral infection, and specific, as well as non-specific responses to drugs. Therefore, reliable tools designed for high spatial resolution, real-time monitoring, and quantification of magnetic signatures and volumetric mass densities of cells will help elucidate the intricate cellular mechanisms.<sup>[5]</sup>

Hitherto, there have been attempts to measure the fundamental material properties of biological living materials with high precision such as the density of single living cells.<sup>[6]</sup> One such technology involves nanofabricated, suspended micro-channel resonators that offer low throughput, and the necessity to use a sophisticated pump mechanism to transfer cells between fluids with different densities.<sup>[5]</sup> Other approaches include phase-shifting interferometry,<sup>[7]</sup> digital holographic

microscopy,<sup>[8]</sup> quadriwave lateral shearing interferometry,<sup>[9]</sup> and quantitative phase tomography.<sup>[10]</sup> Despite its success in quantifying cellular density, this technology has limitations in monitoring subtle morphological changes, manipulating cells, or triggering and quantifying various cellular events without requiring sophisticated fabrication or components. Alternatively, magnetophoresis was used to separate cells based on their native magnetic properties, such as deoxygenated red blood cells (RBCs) from whole blood<sup>[11]</sup> and malaria-infected RBCs from healthy RBCs.<sup>[12]</sup> Magnetic repulsion was also used for label-free separation of cells spiked in magnetic solutions with respect to their size, elasticity, and magnetic property.<sup>[13]</sup> However, these technologies are limited to analyze various cell populations. Moreover, up until now, magnetic levitation has been used for analyses of densities and magnetic susceptibilities of individual, macroscopic objects and as a means effective in: i) separating foods,<sup>[14]</sup> determining the fat content in milk, cheese, and peanut butter, ii) comparing a variety of grains on the basis of their intrinsic densities, iii) guiding self-assembly of objects,<sup>[15,16]</sup> and iv) characterizing forensic-related evidence,<sup>[17]</sup> and noncontact orientation of objects.<sup>[18]</sup> Recently, a method has been demonstrated by using a magnetic levitation approach to measure metal-amplified changes in the density of beads labeled with biomolecules.<sup>[19]</sup> By using gold-nanoparticle-labeled biomolecules, and electroless deposition of gold or silver, change in the density of the beads was observed. These earlier magnetic levitation-based experiments were performed using large setups that had limited compatibility with microscopy.<sup>[16,20]</sup>

Here, we report a simple, yet powerful magnetic levitation-based device (Figure S1, Supporting Information), fully compatible with upright or inverted fluorescence microscopes, which allows real-time, label-free separation, as well as high-resolution monitoring of cell populations. While at current stage this technology does not aim to isolate or purify cell subpopulation, it offers rapid spatial separation of different cell populations based on their unique magnetic and density signatures, without the use of antibody-tagged magnetic beads, centrifugation steps, or the use of a specialized, continuous, or discontinuous density gradient media. The levitation platform enables unique monitoring functional responses of cell populations, i) to a variety of stimuli, ii) over time, and iii) on a cell-by-cell basis.

Negative differences between the magnetic susceptibilities of suspending objects,  $\chi_0$  (e.g., a heterogeneous group of cells) and suspending medium ( $\chi_{\text{medium}}$ ) create a magnetic force field causing objects to be confined at different heights depending on the balance between buoyancy forces and magnetic forces (Figure 1a). Until an object, e.g., an RBC suspended in a paramagnetic medium reaches the equilibrium height, a set of forces, i.e., fluidic drag, inertial, gravitational, and magnetic forces, continuously acts on the object. As the object

Dr. S. Tasoglu,<sup>[†]</sup> Dr. H. C. Tekin, Prof. U. Demirci  
Department of Radiology  
Stanford School of Medicine  
Demirci Bio-acoustic MEMS in Medicine (BAMM) Labs  
Canary Center at Stanford for Cancer Early Detection  
Palo Alto, CA 94304, USA  
E-mail: utkan@stanford.edu



Dr. S. Tasoglu, Dr. H. C. Tekin, Prof. U. Demirci  
Demirci BAMM Labs  
Divisions of Biomedical Engineering  
Infectious Diseases, and Renal  
Department of Medicine  
Brigham and Women's Hospital  
Harvard Medical School  
Boston, MA 02115, USA

J. A. Khoory, Prof. I. C. Ghiran  
Department of Medicine  
Beth Israel Deaconess Medical Center  
Harvard Medical School  
Boston, MA 02115, USA  
E-mail: ighiran@bidmc.harvard.edu

Dr. C. Thomas, Prof. A. E. Karnoub  
Department of Pathology  
Beth Israel Deaconess Medical Center  
Harvard Medical School  
Boston, MA 02115, USA

<sup>[†]</sup>Present address: Department of Mechanical and Biomedical Engineering, University of Connecticut, Storrs, CT 06269, USA

DOI: 10.1002/adma.201405660

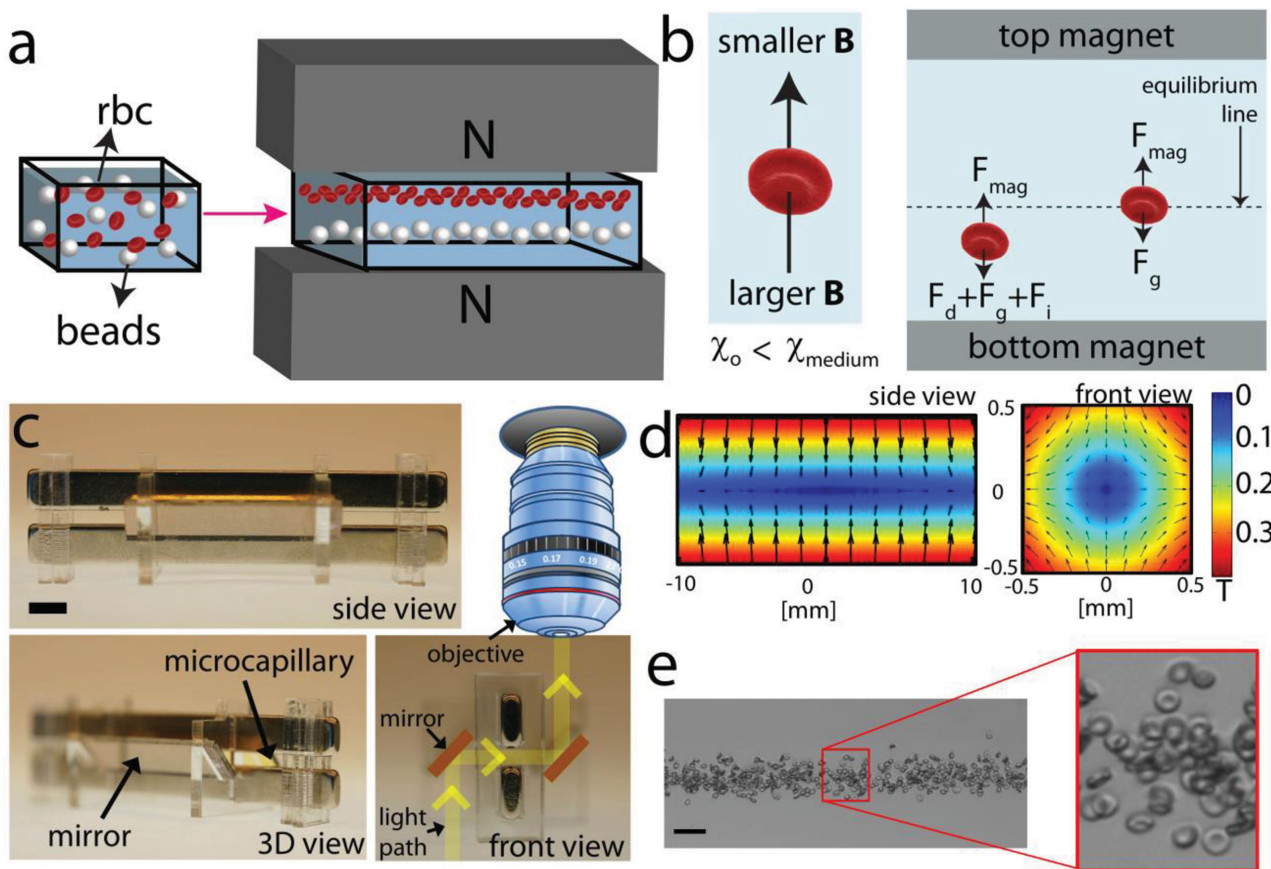


**Figure 1.** Magnetic levitation–based device for static separation, cytometry, and functional interrogation of cells. a) Schematic of the magnetic levitation and cell manipulation in a magnetic field. b) Negative difference between the magnetic susceptibilities of an object ( $\chi_o$ ) and suspending medium ( $\chi_{\text{medium}}$ ) causes the object to move away from a larger magnetic field strength site to lower magnetic field strength. Until the object reaches the equilibrium, fluidic drag ( $F_d$ ), inertial ( $F_i$ ), buoyancy ( $F_g$ ), and magnetic forces ( $F_m$ ) act on the object. As the object gets closer to the equilibrium, its migration velocity, and thus drag and inertial forces, become smaller. c) Front, 3D, and side views of the magnetic levitation setup. A capillary with 1 mm × 1 mm square cross-section is placed between two permanent neodymium magnets (NdFeB) in a configuration where same poles face each other. Scale bar is 3 mm. d) Controlling the position and orientation of objects with magnetic field gradients. Contour plot of the magnetic field for two magnets with same poles facing each other. The magnitude of the magnetic field is constrained between 0 T and 0.4 T. More information on modeling is given in the Supporting Information. e) Confinement of RBCs in the  $50 \times 10^{-3} \text{ M Gd}^{3+}$  solution. Scale bar is 40  $\mu\text{m}$ .

approaches equilibrium, its velocity, and thus drag and inertial forces, become progressively smaller (Figure 1b and Figure S2, Supporting Information). In our experimental setup, a microcapillary tube with a 1 mm × 1 mm square cross-section is placed between two permanent neodymium magnets (NdFeB) in a configuration where same poles face each other. Using this configuration, magnetic forces exerting on the objects oppose the buoyancy forces, allowing objects to levitate at a height that depends on their density. To induce large magnetic forces on the objects, high grade (N52) NdFeB are chosen and they are placed closed to each other (1 mm). Two gold-coated mirrors are placed at each open side of the microcapillary at 45° to create a device compatible with conventional microscopy systems for high-resolution, spatiotemporal monitoring of cells during levitation (Figure 1c). For higher-resolution bright-field and fluorescence imaging (20×, 40×, and 60×), we used a mirror-free setup coupled to a fluorescence upright microscope leveled on its side (see the Experimental Section). Due to the symmetric placement of the two magnets, the symmetric magnetic field

strength distribution with respect to each axis reaching up to 0.4 T (Figure 1d) was achieved. Hence, the suspended cells levitate at a position that depends on: i) the location of minimum field strength and ii) the ratios of the magnetic susceptibility and cellular density. To test our setup, we suspended RBCs isolated from a healthy donor in the  $40 \times 10^{-3} \text{ M}$  gadolinium-based ( $\text{Gd}^{3+}$ ) paramagnetic medium (see the Experimental Section).<sup>[21]</sup> The paramagnetic solution used for all experiments presented here is currently employed for MRI investigations in humans. This medium is nontoxic, iso-osmolar at the concentration used for imaging, and fully compatible with human blood cells (see Figure S3 in the Supporting Information). Following 10 min of magnetic confinement, RBCs stably levitated at a height of approximately 300  $\mu\text{m}$  from the bottom magnet, forming a small, wall-less, blood stream-like assembly that can be easily imaged with high enough resolution to accurately quantify the basic parameters such as, shape, size, optical density, and multi-channel fluorescence of individual cells for post-acquisition image cytometry (Figure 1e).

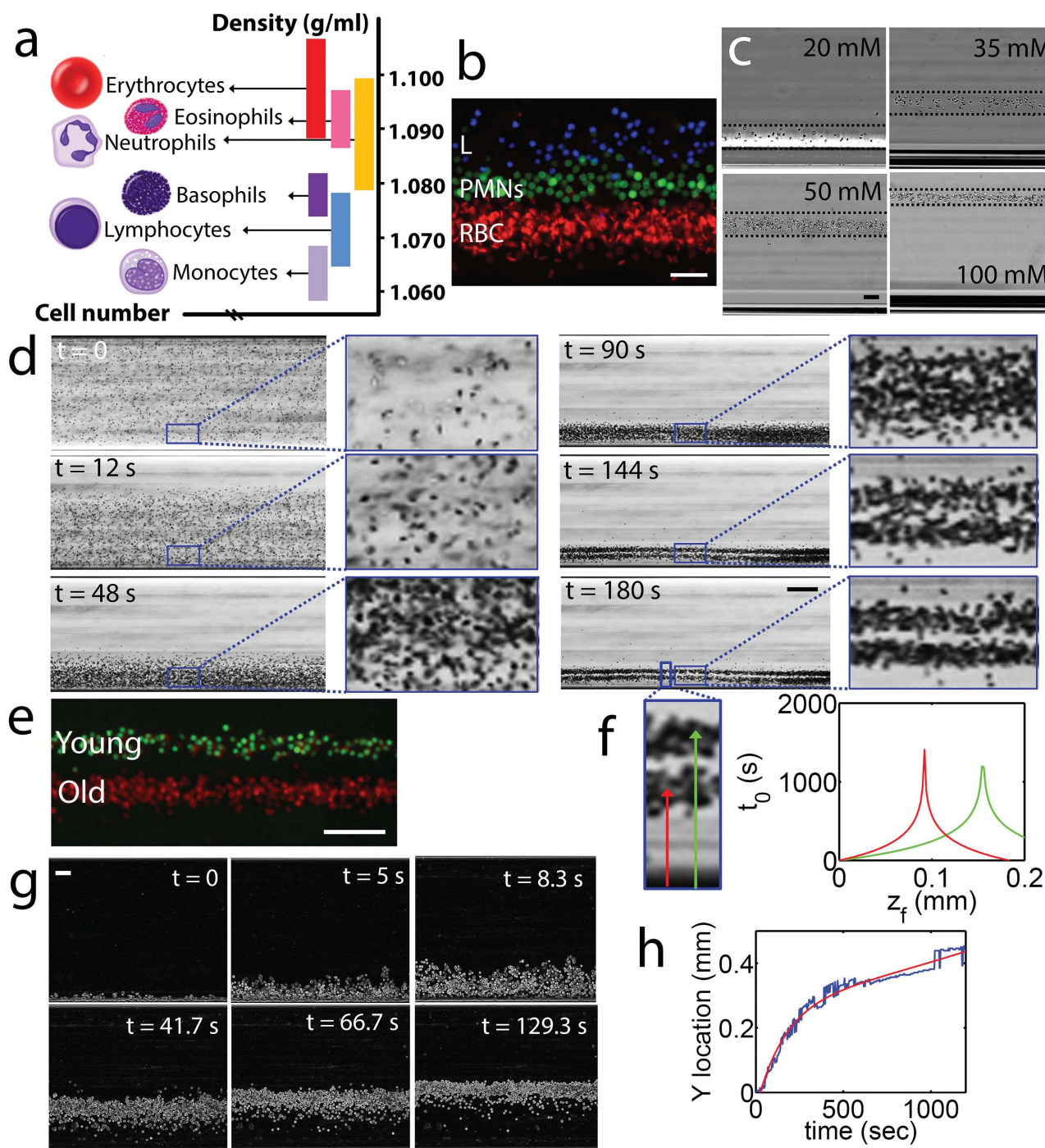


**Figure 2.** Characterization of cell separation using magnetic levitation. a) Density histogram of monocytes, lymphocytes, basophils, PMNs, eosinophils, and RBCs. b) Magnetically driven, density-based separation of fluorescently labeled blood cells. Freshly purified RBCs (RBCs, labeled red), PMNs (PMNs, labeled green), and lymphocytes (L, labeled blue) were mixed and magnetically confined for 15 min in the  $30 \times 10^{-3} \text{ M}$   $\text{Gd}^{3+}$  solution. Scale bar is 40  $\mu\text{m}$ . c) Levitation of RBCs at different molarities of suspending  $\text{Gd}^{3+}$  solution, from left to right: 20, 35, 50, and  $100 \times 10^{-3} \text{ M}$   $\text{Gd}^{3+}$  solution. Scale bar is 40  $\mu\text{m}$ . d) Separation of young and old RBCs by age (Supporting Information, Movie S1). Time-lapse images showing the density separation of a mixed population of purified young and old RBCs. Scale bar is 160  $\mu\text{m}$ . e) Fluorescently labeled young (green) and old (red) RBCs at their equilibrium levitation height. Scale bar is 100  $\mu\text{m}$ . f) Analytical equilibration time as a function of equilibration height of old and young RBCs. g) True magnetic levitation in whole blood (diluted 1:1000). Sedimented RBCs were loaded into the magnetic levitation device and cells imaged for 20 min. Scale bar is 40  $\mu\text{m}$ . h) Time-dependent location of RBCs levitating from bottom surface of microcapillary toward their equilibration point.

Mass density distribution of human blood cells varies between 1.055 and 1.11  $\text{g mL}^{-1}$  (Figure 2a). Volumetric mass density defined as mass per unit volume is one of the most

fundamental physical parameters that characterize a cell. Several cellular events such as differentiation, cell death (apoptosis/necrosis), malignancy, phagocytosis, and cell age cause



permanent or transient changes in cell volumetric mass density. We first assessed the cell-separation resolution of the setup by magnetically focusing previously isolated and fluorescently labeled RBCs (red), polymorphonuclear leukocytes (PMNs) (green), and lymphocytes (blue) (Figure 2b). Our results showed that cells suspended in the  $30 \times 10^{-3}$  M  $\text{Gd}^{3+}$  solution form distinct density, and cell-type specific confinement bands populated by RBCs, PMNs, and lymphocytes alone. Then, we investigated the effect of magnetic strength and density of the suspension solution on the focusing height of RBCs by progressively increasing the molarity of  $\text{Gd}^{3+}$  solution used for RBC suspension (Figure 2c). We found that, as predicted by the formulas presented in the Supporting Information (Equation 11–12c), increases in the molarity of  $\text{Gd}^{3+}$ , and thus magnetic susceptibility of the suspension media, and in a lesser degree of  $\text{Gd}^{3+}$  solution density ( $1.027 \text{ g dL}^{-1}$  at  $100 \times 10^{-3}$  M) caused a gradual increase in the focusing height of RBCs.

RBCs are formed in bone marrow by hematopoietic stem cells (HSCs) and circulate in average for 100–120 d before they are recycled by tissue macrophages. Circulating RBCs through a complement-mediated process continuously release microparticles that progressively decrease their size and surface-to-volume ratio and increase their density.<sup>[22]</sup> To investigate if the sensitivity resolution of the setup was precise enough to separate young ( $1.09 \text{ g mL}^{-1}$ ) from old ( $1.11 \text{ g mL}^{-1}$ ) RBCs based on their different volumetric mass densities, we levitated in a  $30 \times 10^{-3}$  M  $\text{Gd}^{3+}$  solution, a mixture of fluorescently labeled young (green) and old (red) RBCs, which were isolated by Percoll gradient (see the Experimental Section), using our published protocol.<sup>[23]</sup> RBCs, which were initially in a random distribution in the microcapillary, started to focus at different levitation heights when exposed to magnetic field (snapshots of the time lapse recording are shown in Figure 2d) (Supporting Information, Movie S1). Fluorescently labeled young and old RBCs at their respective equilibrium levitation heights are shown in Figure 2e. Using the time-lapse recording of the levitation process, we evaluated analytically the specific equilibrium time function of focusing height of old and young RBCs (Figure 2f). Briefly, equilibrium heights were measured from the bottom magnet for young and old RBCs and were found to be 0.156 mm and 0.092 mm, respectively. Density differences between each cell and suspension liquid were calculated using Figure S2 in the Supporting Information (plotted by Equation 11). By substituting density differences into Equation 14 and 15, equilibrium times were plotted (Figure 2f). Next, we tested the capability of the setup to levitate gravitationally sedimented cells. RBCs were loaded in the glass microcapillary tube and then placed on the bench for 15 min until all cells passively (gravitationally) sedimented along the bottom of the microcapillary. The microcapillary tube was then loaded in the magnetic levitation setup. Due to their relative diamagnetic properties compared to the suspension liquid, cells started to move away from the magnet and levitate toward their density-dependent equilibrium point shown in Figure 2g. We finally quantified the location of cells during magnetic focusing as a function of time using time-lapse microscopy (Figure 2h).

PMNs are phagocytes, i.e., cells capable of sensing and responding to microorganism-specific danger signals followed by specific binding and internalization of foreign

microorganisms or particles. Phagocytic events result in the formation of reactive oxygen species (ROS) and ROS-mediated activation of hydrolytic enzymes. Generation of ROS and reactive nitrogen species (RNS) will cause changes in the magnetic signature of phagocytes, whereas the dynamic interplay between the endocytic and exocytic processes during phagocytosis would directly impact the volumetric mass density of activated PMNs. To test the effect of cell activation on levitation height and cell morphology, we incubated freshly isolated PMNs with phorbol 12-myristate 13-acetate (PMA) ( $10 \times 10^{-9}$  M) for 10 min. As a control, PMNs were left in buffer for 10 min. Cells were then washed, fluorescently labeled, mixed together, and loaded into the magnetic levitation setup. Magnetic focusing revealed distinct differences between control and activated PMNs both in terms of size, shape, optical density, and magnetic and mass density signatures (Figure 3a). Activated PMNs generate intracellular paramagnetic ROS that actively reduces the difference between the magnetic susceptibilities of the cells and the suspending medium. As a consequence, activated PMNs would be expected to “sink” compared to buffer-treated ones. However, our results show that the decrease in density promoted by cell activation<sup>[24]</sup> is more pronounced than the transient increase in magnetic properties and, as a result, the cells levitated to higher elevations than the control. The morphological differences between activated and normal PMNs were evaluated by measuring the roundness of cells, defined as  $\text{perimeter}^2/(4\pi\text{area})$ . Calculated roundness values indicated significant difference between PMA-activated and buffer-treated PMNs (Figure 3c). The same samples were simultaneously examined by flow cytometry for changes in forward and side-scatter properties of PMNs associated with PMA activation (Figure 3d). When compared to flow cytometry, magnetic levitation allows direct visualization of cells, as well as increased shape and size-detection sensitivity and resolution, while simultaneously providing real-time density measurements on a cell-by-cell basis. To further understand the effect of intracellular ROS on the final position of levitating cells, we used cell permeable glutathione (GSH), a known ROS scavenger. Our results showed that GSH-treated PMNs equilibrated slightly below the resting PMNs, whereas activated, low-density PMNs were focused as expected above these two groups (Figure 3e). These results support the hypothesis that ROS potentially changes the magnetic susceptibilities of the cells to an extent in which the levitation heights differ. To test the density resolution of the setup, we next levitated a mixture of PMNs (PMN), lymphocytes (L), and platelets (P). High-magnification imaging of the resting PMNs revealed that, while most of the cells were non-activated, a few (Figure 3f, arrow) showed early signs of activation, through both shape changes and height positions, indicative of lower cell density. In addition, contaminating eosinophils were positioned at the bottom of the PMN column, consistent with their density being equal to or greater than that of the densest PMNs (see Figure 2a). Two hours after continuous levitation, PMNs underwent self-activation<sup>[25]</sup> followed by integrin-mediated homo-typical aggregation (Figure 3g). Of note, some of the PMN clusters also displayed a lower position compared to non-activated PMNs, suggesting that intracellular, paramagnetic ROS species formed during activation also influenced the confinement height of the cells. Next, we studied the relative density changes during human PMN

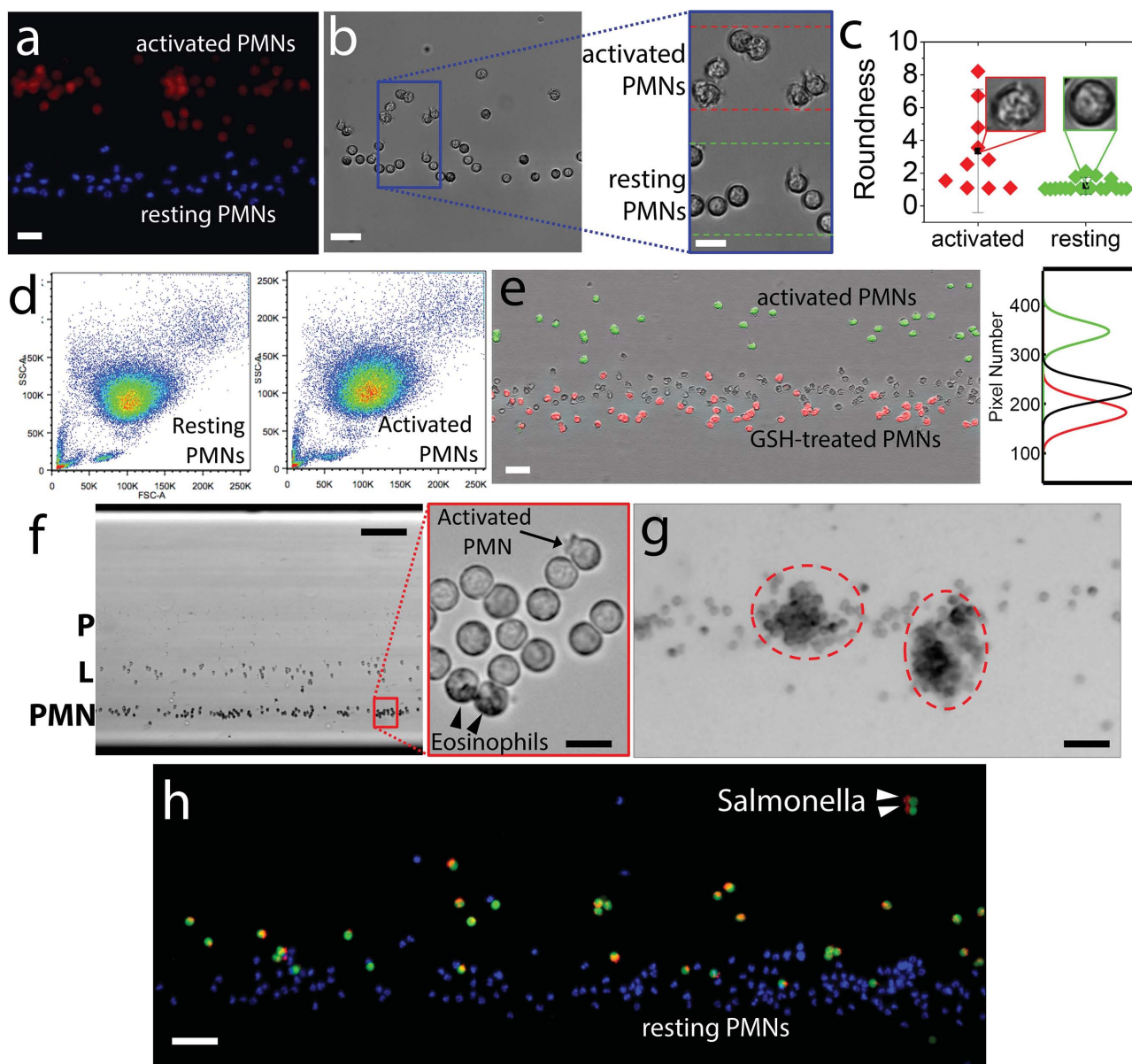


**Figure 3.** Static levitation of functionally altered blood cells. a–c) Changes in PMN density associated with PMA activation. a) Low-magnification fluorescence image of magnetically focused PMNs treated with  $10 \times 10^{-9}$  M PMA (activated PMNs, red) or buffer (resting PMNs, blue). Scale bar is 40  $\mu$ m. b) Low-magnification bright-field image of the levitating PMN. Scale bar is 40  $\mu$ m. Inset, showing the shape and optical density differences between resting and activated PMNs. Scale bar is 20  $\mu$ m. c) Roundness differences between normal and activated PMNs. d) Flow cytometry results for normal PMN (left) and activated PMN with PMA (right). e) Scavenging intracellular ROS alters PMN confinement height. Activated PMNs (green), resting PMNs (unstained), and GSH-treated PMNs (red). Scale bar is 40  $\mu$ m. f) Magnetically driven density separation of blood cells. Left panel, low magnification (4 $\times$ ) of buffy coat cell levitated in  $30 \times 10^{-3}$  M  $Gd^{3+}$  solution for 15 min, showing PMNs (PMN), lymphocytes (L), and platelets (P). Scale bar is 200  $\mu$ m. Right panel, high magnification (40 $\times$ ) of resting PMNs, showing an activated PMN with rough partial outline (arrow) and two eosinophils showing darker granules in the cytoplasm (arrowheads). Scale bar is 20  $\mu$ m. g) Low magnification (10 $\times$ ), 2 h after levitation, PMNs underwent self-activation followed by homo-typical aggregation (red dotted circles). Scale bar is 80  $\mu$ m. h) Phagocytosis of *Salmonella* by human PMNs. Resting PMNs (blue) and PMNs (green) preincubated with Alexa-594-labeled *Salmonella* were mixed, resuspended in  $30 \times 10^{-3}$  M  $Gd^{3+}$  200  $\mu$ L, and magnetically confined for 20 min. Arrowheads point to ingested *Salmonella*. Scale bar is 100  $\mu$ m.

phagocytosis by incubating freshly isolated PMNs with fluorescently labeled *Salmonella montevideo* (Figure 3h). Our results show that phagocytic PMNs have significantly decreased density although there was no clear relationship between the numbers of *Salmonella* ingested (shown as red in Figure 3h) and the confinement height of the PMNs. Our experiments also showed

that labeling the cells with fluorescent dyes did not alter the levitation height of cells (Figure S4, Supporting Information).

To demonstrate the wide applicability of this magnetic levitation-based approach over different cell types, we used circulating cancer cells and sickled RBCs. Metastasis is a process responsible for spreading malignant cells from the primary site

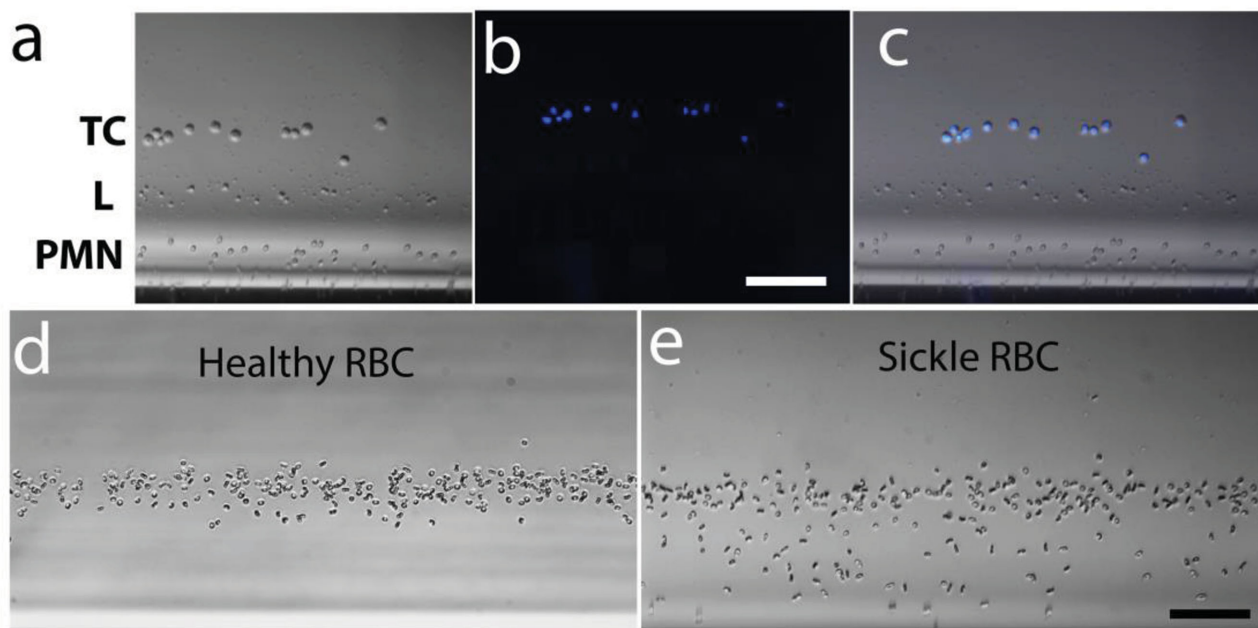


**Figure 4.** Versatility of magnetic levitation-based approach. a–c) Identification of circulating tumor cells in whole blood. Diluted blood isolated from a healthy donor was spiked with breast cancer cells (TC) and magnetically confined using a low ( $15 \times 10^{-3}$  M)  $\text{Gd}^{3+}$  concentration that allows only levitation of TC, PMNs (PMN), and lymphocytes (L) but not that of RBCs. a) Bright-field image of the levitated cells. b) Fluorescent image of the levitated cells. TCs are labeled with blue. c) Merged image of bright-field and fluorescent image. Scale bar is 100  $\mu\text{m}$ . d,e) Identification of sickle cell disease by magnetic levitation. Levitation of: d) healthy and e) sickle RBCs in the presence of  $10 \times 10^{-3}$  M Na metabisulfite. Bright-field images of RBCs recorded after 10 min of confinement. Enhanced (Roberts filter), image analysis-friendly images of the same snapshots are given in Figure S6 (Supporting Information). Scale bar is 100  $\mu\text{m}$ .

to another non-adjacent site. When malignant cells break away from a tumor, they migrate to other areas of the body through the bloodstream or the lymph system, becoming circulating tumor cells (CTC). We prepared a heterogeneous group of cells by spiking normal blood with breast cancer cells (CTC) (Figure 4a) prestained with the cell permeable, DNA-specific dye Hoechst 33342. The cell mixture was then magnetically focused for 15 min in a  $20 \times 10^{-3}$  M  $\text{Gd}^{3+}$  solution that allowed levitation only of PMNs and lymphocytes (L), but not that of RBCs. CTCs were readily identified (nucleus stained blue in Figure 4b, and overlay in Figure 4c) from the multicell suspension being confined close to the center of the microcapillary tube, tens to hundreds of micrometers away from lymphocytes and PMNs, respectively. Although we used a significantly larger number of tumor cells that would normally be found in blood of a patient, the aim of the experiment was to test the device to spatially distinguish blood cells from cells with high genetic and morphological variability such as tumor cell. We also tested the ability of magnetic levitation to provide a binary answer, critical for rapid tests aimed at point of care (POC)-type settings. We levitated and recorded the responses of RBCs isolated from a healthy donor and a patient homozygous (SS) for sickle cell disease in the absence (Figure S5, Supporting Information) or presence of  $10 \times 10^{-3}$  M sodium metabisulfite.<sup>[26]</sup> Our results show that while sodium metabisulfite does not alter the density of healthy RBCs (Figure 4d), RBCs from SS patients fail to maintain their initial densities, rendering a subpopulation of sickle RBCs significantly denser (Figure 4e), displaying a distribution pattern that is both unique and easily quantifiable with standard image analysis methods (Figure S6, Supporting Information).

We have demonstrated the versatility of the magnetic levitation platform that allows spatial separation and activation of cells, as well as monitoring and quantifying of various morphological attributes, specific cellular activities, and agonist responses in real time. The strategy presented here allows also the examination of temporal responses of cells (Figure S7, Supporting Information) that could potentially provide extensive morphological and functional mapping capabilities over time on a cell-by-cell basis for a given population. This device separated cells in a 1 mm capillary, so the cells are spatially enriched in a 3D space. The advantages of the system include: i) simple workflow, ii) lack of sophisticated micro/nano-fabrication components, iii) disposable designs with the possibility of autoclaveable reusable modules, and iv) multidimensional, real-time investigation of dynamic cell:cell communications such as antigen-presenting cell:T cell and platelet:monocyte interactions.<sup>[27]</sup>

Several flow-based microfluidic devices have been developed for isolating and purifying cells in the last decade for numerous applications.<sup>[28]</sup> Here, we did not aim to isolate or purify cell subpopulations. While flow-based microfluidic approaches impart with high throughput, such approaches have to waive a simple yet crucial capability, i.e., real-time spatial and morphological tracking of cell subpopulations and their responses to several factors, e.g., ROS formation or phagocytic events over large time durations. The presented approach here offers rapid spatial separation of different cell populations based on their magnetic signatures and densities without the use of antibody-tagged magnetic beads,<sup>[29]</sup> centrifugation or the use of a specialized, continuous, or discontinuous density gradient media.



The magnetic levitation device offers numerous biotechnology applications, as well as a platform to study and monitor several fundamental cellular behaviors. It provides unique capabilities for cell biology research, where cell densities matter and can reflect various processes such as cell-cycle, phagocytosis, apoptosis, and differentiation. This system is also sensitive to magnetic susceptibilities of cells and can thus be used for analysis of hemoglobin degradation within the RBCs (e.g., stored blood and sickle cells). The capability of monitoring several cellular activities can be also significant for drug discovery, toxicity testing, and single cell testing. Real-time monitoring of levitating cells, followed by protein and nucleic acid analyses, will potentially open avenues for research in unique signaling mechanisms present only during low gravity conditions.

Simplicity, small size scale, and flexibility of the design can potentially make the system compatible with mobile devices for telemedicine and use in resource poor settings for screening and diagnostics of malaria-infected red blood cells and sickle cells. This strategy does not require antibodies, advanced microscopy instrumentation, or techniques for reliable diagnosis, nor the presence of microscopy specialists. The presented magnetic-levitation-based approach provides a broadly applicable tool for high-resolution, real-time cell biology research, as well as for binary disease screening and diagnostics suitable for point-of-care settings.

## Experimental Section

**Antibodies and Reagents:** Hoechst 33342 (H1399, Molecular Probes, Eugene, OR, USA); Hank's balanced salt solution (14025-092), cell mask deep red plasma membrane stain (C10046), cell tracker green, CMFDA (C-7025), NPE-caged ATP (A-1048, Life Technologies, Grand Island, NY, USA); Ficoll (17-5442-03), Percoll (17-0891-01, GE Healthcare, Pittsburgh, PA, USA); citrate 4% w/v (S5770), dextran T500 (31392), glutathione reduced ethyl ester (GSH-ME) (G1404), sodium metabisulfite (S9000), sodium chloride (S5886, Sigma, St. Louis, MI, USA); phorbol 12-myristate 13-acetate (PMA) (1201, Tocris, Bristol, UK); VitroTubes square capillary microcells, borosilicate glass (8100, Vitrocom, Mountain Glass, NJ, USA); gadolinium-based (Gd<sup>3+</sup>) paramagnetic medium Prohance (Bracco Diagnostics, Princeton, NJ, USA); Critoseal (Fisher Scientific, Pittsburgh, PA, USA).

**Magnetic Levitation of Cells:** Cells were resuspended in 200  $\mu\text{L}$  of  $40 \times 10^{-3} \text{ M}$  gadolinium solution unless otherwise noted, all blood cells used were isolated and purified before being diluted (see methods on PBMC, PMN, and RBC isolations in the Supporting Information) into the  $1.0 \text{ mm} \times 1.0 \text{ mm}$  square microcapillary tubes (wall thickness 0.2 mm) by superficial tension action. Critoseal was inserted into either end of the microcapillary to prevent cells from drifting during analysis. The capillary was then loaded into a slot between the magnets and cells were imaged using either QImaging Emc<sup>2</sup> EMCCD camera on an Olympus BX62 microscope or an Qimaging EXi CCD camera on a Zeiss AxioScope microscope. For high-resolution images, we placed a fluorescence microscope leveled on its side perfectly horizontal and used a mirror-free magnetic levitation setup. The images were analyzed with Slidebook 5.5. (3i, Denver, CO, USA), ImageProPlus 7 (Media Cybernetics, Rockville, MD, USA), and iVision 4.7 (Biovision, Exton, PA, USA).

## Supporting Information

Supporting Information is available from the Wiley Online Library or from the author.

## Acknowledgements

I.C.G. and U.D. contributed equally to this work. U.D. acknowledges that this material is based in part upon work supported by the NSF CAREER Award No. 1150733, NIH R01EB015776-01A1, and NIH R21HL112114. I.C.G. acknowledges that this material is based in part upon work supported by the NIH R01 HL096795, NIH R21TW009915, and Bill and Melinda Gates Foundation Award OPP1032683. U.D. is a founder of, and has an equity interest in: i) DxNow, Inc., a company that develops microfluidic and imaging technologies for point-of-care diagnostic solutions, and ii) Koek Biotech, a company that develops microfluidic IVF technologies for clinical solutions. U.D.'s interests were reviewed and are managed by the Brigham and Women's Hospital and Partners HealthCare in accordance with their conflict of interest policies. The authors thank Dr. Peter Weller and Anne-Nicholson Weller for reading the manuscript and helpful comments. S.T., H.C.T., I.C.G., and U.D. declare competing financial interests in the form of a pending provisional patent (BWH Case No. 22697, filed on 02/25/14, "Real-Time, Multidimensional Functional Cellular Interrogation Using a Magnetic Levitation-Based Approach"). Blood was obtained by venipuncture or finger prick from healthy adult volunteers or patients with sickle cell anemia disease in accordance with the guidelines of the Institutional Review Board (IRB) of Beth Israel Deaconess Medical Center and after informed consent in accordance with the Declaration of Helsinki.

Received: December 11, 2014

Revised: March 14, 2015

Published online: June 8, 2015

- [1] D. A. Wolff, H. Pertoft, *J. Cell Biol.* **1972**, 55, 579.
- [2] D. Maric, I. Maric, J. L. Barker, *Methods (Amsterdam, Neth.)* **1998**, 16, 247.
- [3] a) S. J. Martin, J. G. Bradley, T. G. Cotter, *Clin. Exp. Immunol.* **1990**, 79, 448; b) A. H. Wyllie, R. G. Morris, *Am. J. Pathol.* **1982**, 109, 78.
- [4] a) J. E. Mrema, G. H. Campbell, R. Miranda, A. L. Jaramillo, K. H. Rieckmann, *Bull. World Health Organization* **1979**, 57, 133; b) G. P. Rodgers, A. N. Schechter, C. T. Noguchi, *J. Lab. Clin. Med.* **1985**, 106, 30.
- [5] a) W. H. Grover, A. K. Bryan, M. Diez-Silva, S. Suresh, J. M. Higgins, S. R. Manalis, *Proc. Natl. Acad. Sci. USA* **2011**, 108, 10992; b) A. K. Bryan, A. Goranov, A. Amon, S. R. Manalis, *Proc. Natl. Acad. Sci. USA* **2009**; c) A. K. Bryan, V. C. Hecht, W. Shen, K. Payer, W. H. Grover, S. R. Manalis, *Lab Chip* **2014**, 14, 569.
- [6] a) S. Son, A. Tzur, Y. Weng, P. Jorgensen, J. Kim, M. W. Kirschner, S. R. Manalis, *Nat. Methods* **2012**, 9, 910; b) K. Park, L. J. Millet, N. Kim, H. Li, X. Jin, G. Popescu, N. R. Aluru, K. J. Hsia, R. Bashir, *Proc. Natl. Acad. Sci. USA* **2010**, 107, 20691; c) M. Godin, F. F. Delgado, S. Son, W. H. Grover, A. K. Bryan, A. Tzur, P. Jorgensen, K. Payer, A. D. Grossman, M. W. Kirschner, S. R. Manalis, *Nat. Methods* **2010**, 7, 387; d) T. A. Zangle, M. A. Teitell, *Nat. Methods* **2014**, 11, 1221.
- [7] J. Reed, J. Chun, T. A. Zangle, S. Kalin, J. S. Hong, S. E. Pefley, X. Zheng, J. K. Gimzewski, M. A. Teitell, *Biophys. J.* **2011**101, 1025.
- [8] M. Mir, Z. Wang, Z. Shen, M. Bednarz, R. Bashir, I. Golding, S. G. Prasanth, G. Popescu, *Proc. Natl. Acad. Sci. USA* **2011**, 108, 13124.
- [9] a) P. Bon, G. Maucort, B. Wattellier, S. Monneret, *Opt. Express* **2009**, 17, 13080; b) P. Bon, J. Savatier, M. Merlin, B. Wattellier, S. Monneret, *J. Biomed. Opt.* **2012**, 17, 0760041.
- [10] Y. Cotte, F. Toy, P. Jourdain, N. Pavillon, D. Boss, P. Magistretti, P. Marquet, C. Depeursinge, *Nat. Photonics* **2013**, 7, 113.
- [11] a) D. Melville, *Nature* **1975**, 255, 706; b) K.-H. Han, A. Bruno Frazier, *J. Appl. Phys.* **2004**, 96, 5797; c) E. P. Furlani, *J. Phys. D: Appl. Phys.* **2007**, 40, 1313.

- [12] J. Nam, H. Huang, H. Lim, C. Lim, S. Shin, *Anal. Chem.* **2013**, *85*, 7316.
- [13] a) A. R. Kose, H. Koser, *Lab Chip* **2012**, *12*, 190; b) A. R. Kose, B. Fischer, L. Mao, H. Koser, *Proc. Natl. Acad. Sci. USA* **2009**, *106*, 21478; c) F. Shen, H. Hwang, Y. K. Hahn, J.-K. Park, *Anal. Chem.* **2012**, *84*, 3075; d) R. M. Erb, B. B. Yellen, *IEEE Trans. Magn.* **2006**, *42*, 3554.
- [14] K. A. Mirica, S. T. Phillips, C. R. Mace, G. M. Whitesides, *J. Agric. Food Chem.* **2010**, *58*, 6565.
- [15] a) K. A. Mirica, F. Ilievski, A. K. Ellerbee, S. S. Shevkoplyas, G. M. Whitesides, *Adv. Mater.* **2011**, *23*, 4134; b) S. Tasoglu, D. Kavaz, U. A. Gurkan, S. Guven, P. Chen, R. Zheng, U. Demirci, *Adv. Mater.* **2013**, *25*, 1137.
- [16] S. Tasoglu, C. H. Yu, H. I. Gungordu, S. Guven, T. Vural, U. Demirci, *Nat. Commun.* **2014**, *5*, 4702.
- [17] M. R. Lockett, K. A. Mirica, C. R. Mace, R. D. Blackledge, G. M. Whitesides, *J. Forensic Sci.* **2013**, *58*, 40.
- [18] A. B. Subramaniam, D. Yang, H.-D. Yu, A. Nemiroski, S. Tricard, A. K. Ellerbee, S. Soh, G. M. Whitesides, *Proc. Natl. Acad. Sci. USA* **2014**, *111*, 12980.
- [19] A. B. Subramaniam, M. Gonidec, N. D. Shapiro, K. M. Kresse, G. M. Whitesides, *Lab Chip* **2015**, *15*, 1009.
- [20] a) M. B. J. Atkinson, D. K. Bwambok, J. Chen, P. D. Chopade, M. M. Thuo, C. R. Mace, K. A. Mirica, A. A. Kumar, A. S. Myerson, G. M. Whitesides, *Angew. Chem. Int. Ed.* **2013**, *52*, 10208; b) D. K. Bwambok, M. M. Thuo, M. B. J. Atkinson, K. A. Mirica, N. D. Shapiro, G. M. Whitesides, *Anal. Chem.* **2013**, *85*, 8442; c) N. D. Shapiro, K. A. Mirica, S. Soh, S. T. Phillips, O. Taran, C. R. Mace, S. S. Shevkoplyas, G. M. Whitesides, *J. Am. Chem. Soc.* **2012**, *134*, 5637; d) N. D. Shapiro, S. Soh, K. A. Mirica, G. M. Whitesides, *Anal. Chem.* **2012**, *84*, 6166.
- [21] A. Winkleman, K. L. Gudiksen, D. Ryan, G. M. Whitesides, D. Greenfield, M. Prentiss, *Appl. Phys. Lett.* **2004**, *85*, 2411.
- [22] O. Linderkamp, E. Friederichs, T. Boehler, A. Ludwig, *Br. J. Haematol.* **1993**, *83*, 125.
- [23] M. Costa, I. Ghiran, C. K. Peng, A. Nicholson-Weller, A. L. Goldberger, *Phys. Rev. E* **2008**, *78*, 020901.
- [24] S. Pember, K. Barnes, S. Brandt, J. J. Kinkade, *Blood* **1983**, *61*, 1105.
- [25] D. T. Fearon, L. A. Collins, *J. Immunol.* **1983**, *130*, 370.
- [26] T. Asakura, J. Mayberry, *J. Lab. Clin. Med.* **1984**, *104*, 987.
- [27] a) J. E. Freedman, J. Loscalzo, *Circulation* **2002**, *105*, 2130; b) M. L. Dustin, *Semin. Immunol.* **2005**, *17*, 400.
- [28] S. Tasoglu, U. A. Gurkan, S. Wang, U. Demirci, *Chem. Soc. Rev.* **2013**, *42*, 5788.
- [29] S. Wang, S. Tasoglu, P. Z. Chen, M. Chen, R. Akbas, S. Wach, C. I. Ozdemir, U. A. Gurkan, F. F. Giguel, D. R. Kuritzkes, U. Demirci, *Sci. Rep.* **2014**, *4*, 3796.